Nonlinear waves on the surface of a fluid covered by an elastic sheet

Luc Deike†, Jean-Claude Bacri and Eric Falcon

Université Paris Diderot, Sorbonne Paris Cité, MSC, UMR 7057 CNRS, F-75 013 Paris, France

We experimentally study linear and nonlinear waves on the surface of a fluid covered by an elastic sheet where both tension and flexural waves occur. An optical method is used to obtain the full space–time wave field, and the dispersion relation of the waves. When the forcing is increased, a significant nonlinear shift of the dispersion relation is observed. We show that this shift is due to an additional tension of the sheet induced by the transverse motion of a fundamental mode of the sheet. When the system is subjected to a random-noise forcing at large scales, a regime of hydroelastic wave turbulence is observed with a power-law spectrum of the scale, in disagreement with the wave turbulence prediction. We show that the separation between relevant time scales is well satisfied at each scale of the turbulent cascade as expected theoretically. The wave field anisotropy, and finite size effects are also quantified and are not at the origin of the discrepancy. Finally, the dissipation is found to occur at all scales of the cascade, contrary to the theoretical hypothesis, and could thus explain this disagreement.

Key words: elastic waves, turbulent flows, waves/free-surface flows

---

1. Introduction

Wave turbulence theory, or weak turbulence, concerns the dynamical and statistical properties of a set of nonlinear interacting waves (Zakharov, Falkovitch & Lʹvov 1992; Nazarenko 2011; Newell & Rumpf 2011). This theory was developed at the end of the 1960s, and has been applied to various domains: surface waves in oceanography, Rossby waves in the atmosphere, spin waves in magnetic materials, Kelvin waves in superfluid turbulence, and nonlinear optics. It assumes strong hypotheses such as those addressing weakly nonlinear, isotropic and homogeneous random waves in an infinite size system with scale separation between injection and dissipation of energy. It notably predicts analytical solutions for the spectrum of a weakly nonlinear wave field at equilibrium or in a stationary out-of-equilibrium regime. So far, a few well-controlled experiments on wave turbulence have been designed to specifically test the theory and its limitations. They mainly concern capillary–gravity waves on the surface of a fluid (Wright, Budakian & Putterman 1996; Denissenko, Lukaschuk & Nazarenko 2007; Falcon, Laroche & Fauve 2007; Kolmakov *et al.* 2009; Herbert, Mordant & Falcon 2010; Xia, Shats & Punzmann 2010; Cobelli *et al.* 2011), elastic waves on a metallic plate (Boudaoud *et al.* 2008; Mordant 2008), and nonlinear optics

† Email address for correspondence: luc.deike@univ-paris-diderot.fr

(Laurie *et al.* 2012). Experimental studies of wave turbulence on new systems are thus of great interest, notably to test the domain of validity of the theory in experiments.

Here, we present a well-controlled experiment to study nonlinear interacting waves on the surface of an elastic sheet covering the surface of a fluid. Two types of hydroelastic waves occur: tension waves and flexural (or bending) waves that result from the coupling of the elastic sheet response to that of the fluid underneath. The main motivation is to study wave turbulence in this new system that enables the dispersion relation of waves to be tuned by controlling the elastic sheet tension applied.

It is noteworthy that the response of a thin elastic sheet covering a fluid to a dynamical perturbation usually generates hydroelastic surface waves occurring in various settings: bio-medical applications such as heart valves (Grotberg & Jensen 2004), flapping flags (Shelley & Zhang 2011) and industrial applications like very large floating structures (Watanabe, Utsunomiya & Wang 2004). In oceanography, flexural–gravity waves are known to propagate on the surface of lakes or oceans covered by ice and are involved in various ice floe phenomena (Takizawa 1985; Squire *et al.* 1988; Squire, Hosking & Kerr 1996; Dias 2002; Squire 2007). Such waves are governed by the same wave equation as the one presented here. However, this analogy is quite limited since the free floating boundary condition in ice floes is not respected here, and also the orders of magnitude in ice floes lead to the predominance of flexural–gravity waves instead of the flexural–tension waves here.

The paper is organized as follows. The theoretical background is presented in §2. The linear equations and the boundary conditions of an elastic sheet covering a fluid are recalled. The relation between an applied pressure to the sheet and the induced static tension is then given. The nonlinearities in the system are discussed as well as their implications for wave interactions processes. Dimensional analysis of wave turbulence is then presented for the case of tension and flexural waves on the surface of a fluid covered by an elastic sheet. In §3, the experimental setup is presented. The optical techniques to measure the wave field are introduced, and so is the tuning of the static tension of the sheet by an applied hydrostatic pressure. Results are presented in §§4 and 5. In §4, observations of tension and bending waves over two decades in frequency are described, in good agreement with the theoretical dispersion relation of linear waves. When the wave amplitude is increased, a shift of the dispersion relation occurs. We show that this shift is due to the dynamics of slow nonlinear waves (fundamental eigenmode of the sheet) that induces an additional quasi-static tension to the sheet. Observations of the wave turbulence regime are then presented in §5. The spectrum of the wave transverse velocity is found to scale as a power law of both the frequency and wavenumber, both power-law exponents being in disagreement with the ones predicted by wave turbulence theory. We then show that wave anisotropy exists but is not at the origin of this discrepancy. The dissipation time of the waves, the nonlinear interaction time and the linear time of wave propagation have been measured at each scale, and show that the time scale separation hypothesis of wave turbulence theory is fulfilled. On the other hand, dissipation is found to occur at all scales, contrary to the theoretical hypothesis, and could thus explain this disagreement for the spectrum scaling. The conclusions are drawn in §6.

2. Theoretical background

2.1. *Linear dispersion relation*

Assume a floating elastic sheet subjected to an uniform and isotropic tension T. Properties of the sheet are: density ρ_e, Young modulus E, Poisson modulus ν, and

thickness h. The fluid density is ρ and its depth beneath the sheet at rest H. The momentum equation of the thin elastic sheet is then given by (Landau & Lifchitz 1951; Davys, Hosking & Sneyd 1985; Schulkes, Hosking & Sneyd 1987)

$$D\nabla^4\eta - T\nabla^2\eta + \rho_e h\frac{\partial^2\eta}{\partial t^2} = p, \qquad (2.1)$$

with η the vertical sheet deformation, p the pressure due to the liquid on the elastic sheet, $D \equiv Eh^3/12(1 - \nu^2)$ the bending modulus of the elastic sheet, $\nabla^2 \equiv \partial^2/\partial x^2 + \partial^2/\partial y^2$, and $\nabla^4 \equiv \partial^4/\partial x^4 + \partial^4/\partial y^4 + 2\partial^4/\partial x^2\partial y^2$ the Laplacian and bi-Laplacian operators. Considering an irrotational flow of velocity potential $\phi(x, y, z, t)$, the pressure equation on the surface $z = \eta$ is given by $p = -\rho(\partial\phi/\partial t)_{z=\eta} - \rho g\eta$, with g the acceleration due to gravity. For a plane wave solution, using the kinematic boundary condition on the sheet surface $\partial\eta/\partial t = (\partial\phi/\partial z)_{z=\eta} = \tanh kH(\phi)_{z=\eta}$, and assuming negligible sheet inertia ($\rho_e kh/\rho \ll 1$) and infinite depth ($kH \gg 1$), the linear dispersion relation reads (Schulkes *et al.* 1987)

$$\omega^2 = gk + \frac{T}{\rho}k^3 + \frac{D}{\rho}k^5. \qquad (2.2)$$

It involves three terms: a gravity one, and two elastic ones. The second term of the right-hand side of (2.2) is a tension term structurally analogous to a capillary term (Lamb 1932), whereas the third term corresponds to bending. Note that the dispersion relation for pure elastic waves on a plate is $\omega^2 \sim Tk^2 + Dk^4$ (Landau & Lifchitz 1951), equation(2.2) coming from the coupling of the sheet elasticity with the liquid underneath. The cross-over between the various wave regimes in (2.2) can be evaluated, for typical values of the applied tension $T \approx 4$ N m^{-1} and of the bending modulus $D \approx 5 \times 10^{-6}$ N m of the latex sheet used here (see § 3). Balancing the first and second terms of the right-hand side of (2.2) gives the transition between gravity and tension waves, $\lambda_{gT} = 2\pi\sqrt{T/(g\rho)} \simeq 10$ cm; balancing the second and third terms gives the transition between bending and tension waves, $\lambda_{TD} = 2\pi\sqrt{D/T} \simeq 1$ cm. Note that for ice floes, the bending elastic term prevails over the tension one, and the order of magnitude of the flexural–gravity transition is $\lambda_{gD} = 2\pi[D^\star/(g\rho)]^{1/4} \simeq 100$ m for a typical ice bending modulus $D^\star \approx 10^9$ N m (Davys *et al.* 1985; Schulkes *et al.* 1987).

2.2. *Boundary conditions and sheet eigenmodes*

Let us consider an elastic sheet clamped over the top of a vertical circular vessel of radius R. The boundary condition is thus $\eta(R) = 0$ (and consequently $\partial\eta(R)/\partial t = 0$). In such a circular geometry, the sheet eigenmodes are given by the zeros of the Bessel functions: $J_n(kR) = 0$, with J_n a Bessel function of the first kind, n an integer and k the eigenmode wavenumber (Morse & Ingard 1968). The first symmetric and antisymmetric eigenvalues are $J_0(kR) = 0$ leading to $k_{0,1}R = 2.405$, and $k_{0,2}R = 5.520$ and $J_1(kR) = 0$ leading to $k_{1,1}R = 3.832$ and $k_{1,2}R = 7.016$. The corresponding natural frequencies are then obtained using the dispersion relation (2.2). Note that in the case of an ice floe, the ice boundary is free to move and free edge boundary conditions have to be considered, ($\partial\eta(R)/\partial t = 0$ and vanishing of the bending moment, see Squire *et al.* (1996)).

2.3. *Scaling of tension with pressure: static case*

An external pressure P_s applied on an elastic sheet clamped over the top of a circular vessel generates a static tension T_s of the sheet. T_s is analytically computed as a function of P_s as follows. When P_s is applied, the sheet deforms, and for large

enough deformation (maximum deflection $\eta_m \gg h$), the tension term prevails over the bending one in (2.1) (Landau & Lifchitz 1951). Under the assumption of an homogeneous and isotropic stress tensor, the static force equilibrium can be written as $T_s \nabla^2 \eta = P_s$ (Landau & Lifchitz 1951). Using the circular boundary condition $\eta(R) = 0$, the deformed solution for a sheet of radius R is a parabolic surface $\eta(r)$ (Landau & Lifchitz 1951)

$$\eta(r) = \frac{P_s}{4T_s}(R^2 - r^2). \tag{2.3}$$

The maximum deflection of the parabola is thus

$$\eta_m \equiv \eta(0) = P_s R^2 / (4T_s). \tag{2.4}$$

Under the above hypotheses and using Landau & Lifchitz (1951) the dependence between P_s and T_s can be calculated:

$$T_s = \left[\frac{Eh}{32(1-\nu)} P_s^2 R^2 \right]^{1/3}. \tag{2.5}$$

2.4. *Nonlinear resonant interactions*

Nonlinearities involved in the system can be introduced either in the equations of the elastic plate, or in the ones of the fluid, or in the boundary condition between the fluid and the plate. A complete discussion of the corresponding equations can be found in Peake (2001) and Peake & Sorokin (2006). Although the equation for a single elastic plate involves cubic nonlinearities, the pressure term and the boundary condition between the fluid and the plate involve quadratic nonlinearities. The pressure term is

$$p(x, y, t) = \rho g \eta + \frac{\partial \phi}{\partial t} + \rho \frac{v^2}{2}, \tag{2.6}$$

with $\eta(x, y, t)$ the wave height, and $v(x, y, t) = \partial \eta / \partial t$ the transverse wave velocity. The importance of the nonlinear term in the pressure will be shown experimentally in §4. Thus, the coupling between the fluid and the elastic plate involves a quadratic nonlinearity of the pressure term.

When considering resonant wave interactions, 3-wave interactions occur when quadratic nonlinearities are present in the system while 4-wave interactions have to be considered in the case of cubic nonlinearities (Zakharov *et al.* 1992; Nazarenko 2011). The dynamics of wave interactions is dominated by the lowest nonlinear order (Zakharov *et al.* 1992; Nazarenko 2011). Thus, when 3-wave and 4-wave interactions occur as in our case, 4-wave interactions are generally neglected. Thus, only 3-wave interactions need be considered here. The 3-wave interactions also have to be compatible with the dispersion relation. In our case, the dispersion relation of tensional and bending waves is of decay type, i.e. $\omega \sim k^\mu$ with $\mu > 1$ (as for capillary waves), and thus fulfils the 3-wave resonant conditions on the frequency ($\omega_1 \pm \omega_2 \pm \omega_3 = 0$) and on the wavenumbers ($k_1 \pm k_2 \pm k_3 = 0$). A kinetic equation assuming 3-wave interactions has been proposed in the case of a floating ice sheet on water (Marchenko & Shrira 1991). Note also that in the case of pure flexural wave turbulence on an elastic plate (without water), 4-wave interactions are considered since the nonlinearities of the plate are cubic (Düring, Josserand & Rica 2006). For pure gravity waves, nonlinearities are

quadratic but 3-wave interactions are not possible since the resonant conditions are not satisfied due to the geometry of the dispersion relation ($\mu < 1$), and only 4-wave interactions have to be considered (see McGoldrick *et al.* 1966 and references therein).

2.5. *Dimensional analysis in wave turbulence*

One of the main results of wave turbulence theory is the existence of out-of-equilibrium stationary solutions of the kinetic-like equation for the wave action spectrum $n_k = E_k/\omega$, with E_k the wave energy spectrum in the Fourier space. The kinetic equation is generally written (Zakharov *et al.* 1992; Nazarenko 2011; Newell & Rumpf 2011):

$$\frac{\partial n_k}{\partial t} = St(n_k) + F_k - \Gamma_k n_k, \tag{2.7}$$

where $St(n_k)$ is the collision integral which depends on the physical properties of the propagation medium and on the type of nonlinear wave interaction, F_k is the forcing term, and Γ_k the dissipative rate. Energy conservation leads to a stationary solution in the form of a direct energy cascade from the injection scale k_i to the dissipation scale k_d, the cascade inertial range being defined by the scale separation hypothesis $k_i \ll k \ll k_d$ in a similar way to hydrodynamic turbulence. The other main hypothesis used to derive the wave turbulence spectrum is an infinite medium, local interactions, an homogeneous and isotropic wave field, weak nonlinearities and the following time scale separation: $\tau \ll \tau_{nl} \ll \tau_d$, with $\tau = 1/\omega$ the linear propagation time, τ_{nl} the nonlinear wave interaction time and τ_d the dissipation time (Zakharov *et al.* 1992; Nazarenko 2011; Newell & Rumpf 2011).

Under the above hypothesis, dimensional analysis can be performed in wave turbulence as presented by Connaughton, Nazarenko & Newell (2003) in order to determine stationary solutions of the kinetic equation. For a given dispersion relation $\omega = ck^\mu$, the wave energy spectrum of a set of nonlinear waves is supposed to be a self-similar function of the scale k, the flux of the conserved quantity and the constant c. Here, a direct cascade of energy is considered and the flux through the scales is the energy flux per mass density, ϵ (dimension $[L^3 T^{-3}]$). Experimentally, the quantity of interest here is the power spectrum of wave vertical velocity, $S_v(k)$ (dimension $[L^3 T^{-2}]$) which is assumed to be given by

$$S_v(k) \sim \epsilon^{1/(N-1)} c^\beta k^\alpha, \tag{2.8}$$

with N the number of interacting waves in the leading process. The dependence $S_v(k) \sim \epsilon^{1/(N-1)}$ is given by wave turbulence theory (Zakharov *et al.* 1992; Connaughton *et al.* 2003; Nazarenko 2011). As explained above in §2.4, $N = 3$ is considered in our case. For tensional waves in deep water, one has $\omega^2 = (T/\rho)k^3$, and obtains dimensionally

$$S_v^t(k) \sim \epsilon^{1/2} \left(\frac{T}{\rho}\right)^{1/4} k^{-3/4}, \tag{2.9}$$

which is analogous to the case of capillary waves. For bending waves in deep water, one has $\omega^2 = (D/\rho)k^5$, and one obtains dimensionally

$$S_v^b(k) \sim \epsilon^{1/2} \left(\frac{D}{\rho}\right)^{1/4} k^{-1/4}. \tag{2.10}$$

Similarly, one obtains the frequency spectra of the wave height (dimension $[L^2T]$) as

$$S_\eta^t(f) \sim \epsilon^{1/2} \left(\frac{T}{\rho}\right)^{1/6} f^{-17/6} \quad \text{and} \quad S_\eta^b(f) \sim \epsilon^{1/2} \left(\frac{D}{\rho}\right)^{1/10} f^{-27/10}. \tag{2.11}$$

The scaling of the nonlinear interaction time is determined by balancing the left-hand side and the collision integral of (2.7), $1/\tau_{nl} \sim St(n_k)/n_k$ (Newell, Nazarenko & Biven 2001; Connaughton *et al.* 2003). Using (2.9) and the dimensional structure of the collision integral for 3-wave interactions for tensional waves, leads to

$$1/\tau_{nl} \sim \epsilon^{1/2} \left(\frac{T}{\rho}\right)^{-1/4} k^{3/4}, \tag{2.12}$$

while for bending waves:

$$1/\tau_{nl} \sim \epsilon^{1/2} \left(\frac{D}{\rho}\right)^{-1/4} k^{1/4}. \tag{2.13}$$

3. Experimental setup

The experimental setup is shown in figure 1(*a*). It consists of a cylindrical vessel of radius $R = 10$ cm (or 20 cm) filled with water up to a height $H = 43$ cm (or 20 cm, respectively). An elastic latex sheet is stuck on the circular top of the container. We carefully checked that no air bubbles are trapped between the sheet and the water. Measured physical properties of the latex sheet are: thickness $h = 0.35$ mm (or 0.5 mm), Young modulus $E = 1.05 \times 10^6$ N m^{-2} (or 1.5×10^6 N m^{-2}, respectively), and Poisson modulus $\nu \approx 0.5$ (industrial latex was provided by Carrat and Eurocatsuits). Waves on the sheet are generated by the vertical motion of a rectangular wave maker (75 mm × 10 mm, or 186 mm × 10 mm) driven by an electromagnetic shaker (LDS V201 or LDS V406) as shown in figure 1(*a*). The shaker is driven by a sinusoidal forcing at frequency f_p (with $f_p \in [10:50]$ Hz) or by a random-noise forcing band-pass filtered around f_p within a frequency bandwidth $f_p \pm \Delta f$ (with $f_p \in [8:15]$ Hz and $\Delta f = 1.5$ Hz). A stationary wave field state is reached after a few seconds and measurements are done during the steady state. The full three-dimensional space–time wave field is measured using a fast Fourier profilometry technique (Cobelli *et al.* 2009), recently used on elastic waves on a metallic plate (Mordant 2010) or for gravity–capillary waves on a fluid surface (Herbert *et al.* 2010; Cobelli *et al.* 2011). Fringes with inter-fringe distances of 1 mm are projected on the sheet surface by a high-resolution video-projector (Epson TW3000), and the space–time evolution of the fringe deformations allows the reconstruction of the velocity normal to the free surface $v(x, y, t)$ with a fast camera (Phantom V9) recording at 1000 f.p.s. for $\mathcal{T} = 4$ s. The size of the recorded images, centred in the middle of the sheet, is 10 cm × 8 cm for the small vessel, and 25 cm × 20 cm for the large one. A typical reconstructed pattern of $v(x, y, t)$ is shown at a given time in figure 1(*b*). From the movie of $v(x, y, t)$, one computes the power spectrum density of transverse velocity $S_v(k_x, k_y, f)$ from multidimensional Fourier transforms. By integrating $S_v(\boldsymbol{k}, f)$ over all directions of the wave vector $\boldsymbol{k}$, we also obtain $S_v(k = \|\boldsymbol{k}\|, f)$, with $k \equiv \sqrt{k_x^2 + k_y^2}$ the wavenumber. The transverse velocity of the wave at a fixed location was also directly recorded with a Doppler velocimeter (Polytech OPV 506) for long times, $\mathcal{T} = 300$ s, to measure the slow response of the system. The wave-maker velocity $V(t)$ is measured by an
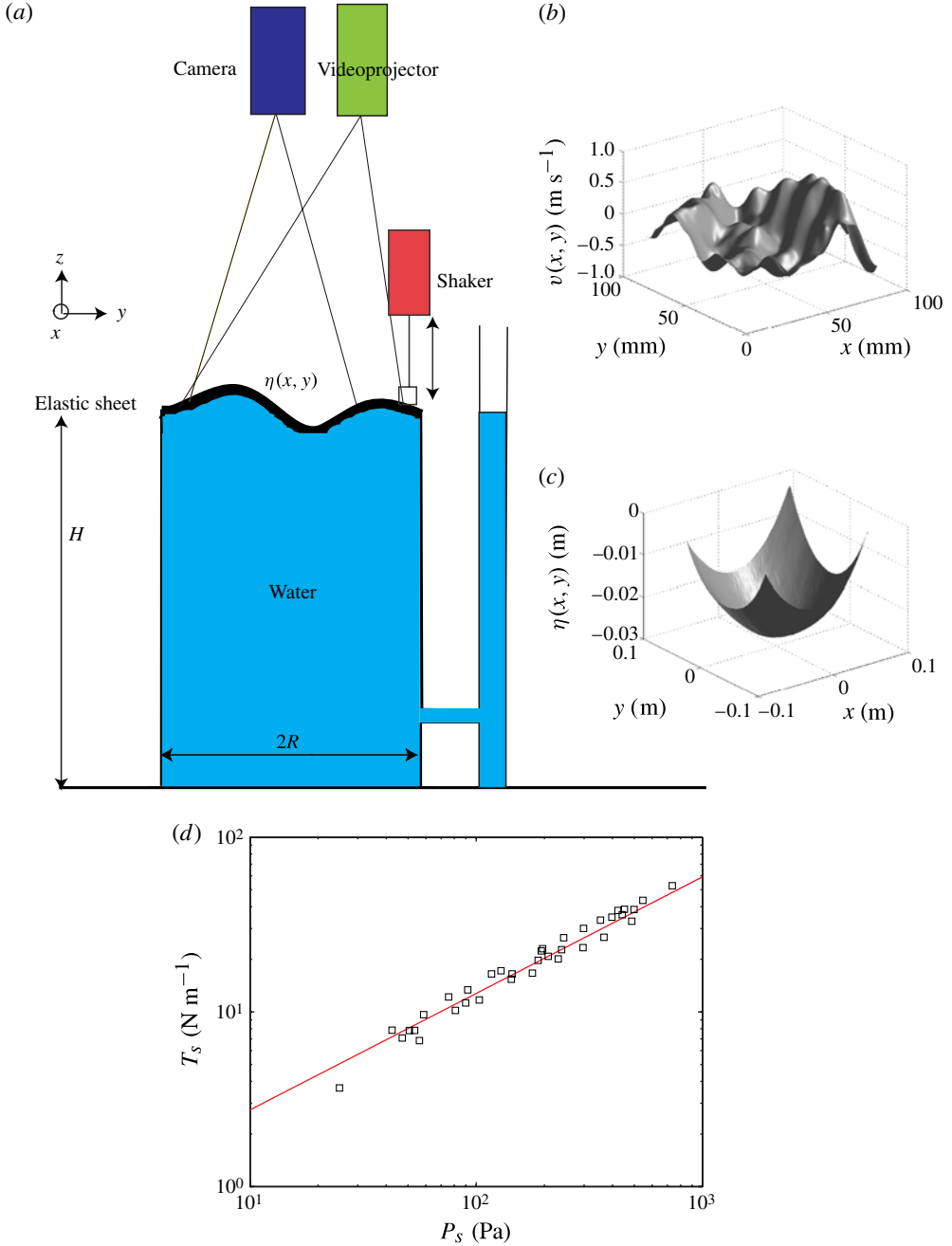
(*a*)

(*b*)

(*c*)

(*d*)

FIGURE 1. (Colour online) (*a*) Experimental setup. (*b*) Typical wave transverse velocity $v(x, y)$ reconstructed by Fourier transform profilometry. (*c*) Reconstructed height profile of the sheet for $P_s = -130$ Pa showing a parabolic static profile. (*d*) Static tension T_s as a function of the applied pressure $|P_s|$. Solid line corresponds to (2.5), $T_s = [(Eh/32(1 - v))P_s^2 R^2]^{1/3}$.

accelerometer (BK 4393) fixed on the wave maker and the force $F(t)$ applied by the wave maker on the sheet is measured by a piezoelectric sensor (FGP 10 daN). The mean power I injected into the system is then evaluated by $I = \int_0^{\mathcal{T}} F(t)V(t)\,dt/\mathcal{T}$ (Falcon 2010).

As shown in figure 1(*a*), the vessel is connected through a small pipe to a vertical tube that enables the control of the hydrostatic pressure P_s imposed on the elastic sheet by adding or removing an amount of water from the tube. When the water inside the vertical tube is at the same height as the sheet, $P_s = 0$. By filling (or draining) the tube of water, changing the height by ΔH, an external positive (or negative) pressure is applied since the sheet is stuck on the top of the vessel. As shown in figure 1(*c*), the elastic sheet has a parabolic shape well described by (2.3), and its maximum deflection η_m can be then measured. The hydrostatic pressure is then estimated by $P_s = \rho g(\Delta H - \eta_m)$, since the pressure difference between the top and the bottom of the parabola is negligible. Note that this condition is needed to consider a constant pressure over the whole elastic sheet. For various applied P_s, we measure η_m, and experimentally deduce the corresponding static tension T_s on the sheet from (2.4). As shown in figure 1(*d*), T_s is found to evolve with P_s in good agreement with (2.5) with no fitting parameter during this comparison. Note that the depression or overpressure cases are similar since the weight of the sheet is negligible for our range of P_s. Thus the absolute value of P_s will be given in the following. The initial static tension T_s on the sheet is thus well controlled by the applied static pressure P_s. This allows us to study the linear and nonlinear properties of waves on a floating elastic sheet with a tunable tension.

The pressure only due to the weight of the elastic sheet with no water beneath is $P_s^0 = \rho_e g h$. One can experimentally obtain from (2.4) the static tension T_s^0 of the elastic sheet due to its attachment to the vessel without water. One finds $T_s^0 \simeq 2\text{--}4$ N m^{-1} whatever the elastic sheets and container sizes used. This value will correspond to the minimal value of static tension reached when water is added and no hydrostatic pressure applied. Thus, one considers $P_s = P_s^0$ and $T_s = T_s^0$ in this case. As pointed out in § 2.1, for $T_s^0 \approx 4$ N m^{-1}, the transition between gravity and tensional waves is $\lambda_{gT} \simeq 10$ cm, of the order of the vessel size and the observation window. Thus, only elastic waves will be observed here. Moreover, bending waves will occur for wavelengths smaller than $\lambda_{TD} \simeq 1$ cm. In a prestressed case, T_s is increased and these transitions evolve as $\lambda_{gT} \sim \sqrt{T_s}$ and $\lambda_{TD} \sim 1/\sqrt{T_s}$ (see § 2.1). Thus, almost only tensional waves will be observed in the case of a large initial tension: for instance, if $T_s = 10$ N m^{-1}, $\lambda_{gT} \simeq 20$ cm and $\lambda_{TD} \simeq 0.4$ cm.

4. Dispersion relation of nonlinear waves

Here, we characterize experimentally the dispersion relation of waves when the system is subjected to either a monochromatic or a filtered random-noise forcing.

4.1. *Dispersion relation*

The space–time power spectrum $S_v(k, f)$ of the transverse velocity of waves is shown figure 2 for two forcing amplitudes, and for $P_s = 0$. In both cases, the wave energy injected at low frequencies is transferred through the scales towards high frequencies by nonlinear interaction between waves. The wave energy is mainly localized on a single curve in the ($\omega \equiv 2\pi f$, $k \equiv 2\pi/\lambda$) space that corresponds to the nonlinear wave dispersion relation. Theoretical dispersion relations of both pure tension waves, $\omega^2 = (T/\rho)k^3$, and of tension and bending waves, $\omega^2 = (D/\rho)k^5 + (T/\rho)k^3$, are plotted
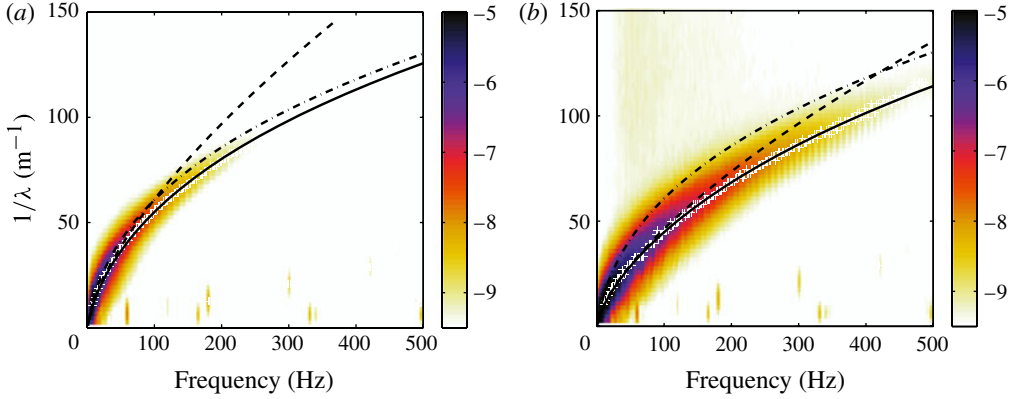
FIGURE 2. (Colour online) Space–time spectrum $S_v(k, f)$ of the transverse velocity of waves for: (*a*) moderate ($p = 12$ Pa) and (*b*) strong ($p = 33$ Pa) forcing amplitudes. Random forcing bandwidth: 8.5 ± 1.5 Hz in (*a*). Colours are log scaled. $P_s = 0$. The $+$ symbols correspond to the local maxima of $S_v(k, f)$ for each frequency; dashed lines are $\omega^2 = (T/\rho)k^3$; solid lines are $\omega^2 = (D/\rho)k^5 + (T/\rho)k^3$; dash–dot lines are $\omega^2 = (D/\rho)k^5 + (T_s^0/\rho)k^3$. Fitting parameter: $T = $ (*a*) 7 and (*b*) 16 N m^{-1}. $f^* = 20$ Hz and $1/\lambda^* = 20$ m^{-1} from (2.2).

in figure 2 with T the single fitting parameter, as well as the dispersion relation for the tension equal to the static tension $T = T_s^0$. When both elastic terms are taken into account, the theoretical dispersion relation describes the experimental results well over the whole frequency range. Tension waves occur mainly at low frequencies whereas bending waves occur at higher frequencies as expected. When the forcing amplitude is increased (see figure 2*b*), wave interactions still redistribute the wave energy on the dispersion relation up to higher frequencies, but with two main differences. First, the width of the dispersion relation is broader in the f and k directions. Second, a shift of the dispersion relation is observed, the fitting value of T being more than doubled when the forcing is increased by a factor 3. Thus, the observed nonlinear dispersion relation follows the linear predicted one with a tension that depends on the forcing amplitude.

4.2. *Shift of the dispersion relation*

Let us now introduce a dynamical pressure p due to the wave field that will correspond to a mean 'dynamical' tension T on the interface. The dynamical pressure of the wave field on the interface is given by (2.6) and is estimated as: $p(x, y, t) = \rho g \sigma_\eta + \rho \sigma_v^2/2$, where σ_η and σ_v are the r.m.s. values of $\eta(x, y, t)$ and $v(x, y, t)$ such that $\sigma_X \equiv \int_0^{\mathscr{T}} \sqrt{\langle (X - \langle X \rangle)^2 \rangle}\,\mathrm{d}t/\mathscr{T}$, where $\langle \cdot \rangle$ denotes two-dimensional spatial averaging on (x, y), and $\mathscr{T}$ is the total recording time. Since the system is stationary, the time-dependent term in (2.6) vanishes. Moreover, we have checked that p is proportional to the mean power I injected by the wave maker within the system. We find $p = bIf_p$ for our range of forcing frequencies f_p, with b a dimensional constant depending on the forcing shape (sinusoidal or random). Thus, p will control the forcing amplitude in the following. One can now compare the influence of the hydrostatic pressure, P_s, and of the dynamical one, p, on the dispersion relation of the waves.

Figure 3(*a*) shows the dispersion relation extracted from the maxima of the spectrum $S_v(k, f)$ for each scale, for various forcing amplitudes, and for $P_s = 0$. A significant
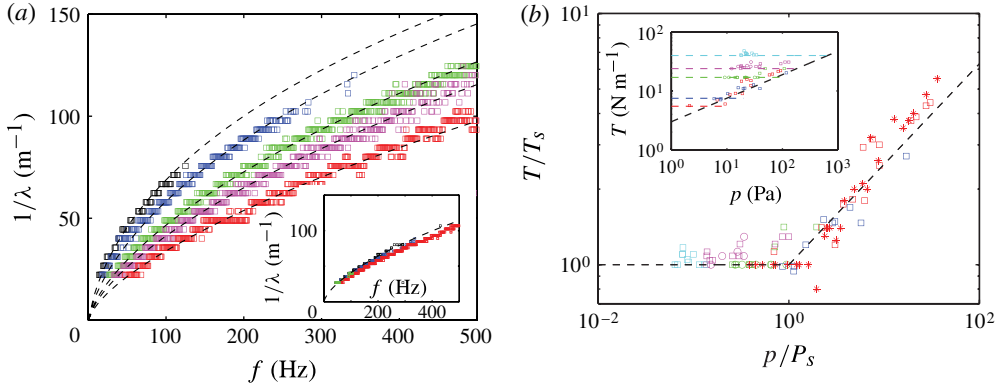
FIGURE 3. (*a*) Dispersion relations when the forcing amplitude is increased: p goes from 3 (top) to 100 (bottom) Pa, $P_s = 0$. Dashed lines correspond to $\omega^2 = (D/\rho)k^5 + (T/\rho)k^3$ with T the only fitting parameter: $T = 4$ to 40 N m^{-1} (from top to bottom). Inset: same as main figure but with $P_s = 130$ Pa ($T_s = 22$ N m^{-1}), and $10 \leqslant p \leqslant 130$ Pa. Dashed line, best fit: $T = 22$ N m^{-1}. (*b*) T/T_s as a function of p/P_s, for various $P_s =$ (red square) P_s^0, (blue square) 7, (green square, circle) 55, (magenta square, circle) 130, (cyan square, circle) 274 Pa for $R = 10$ cm, and $P_s = P_s^0 = 4$ (red star) Pa for $R = 20$ cm. These values correspond, from (2.5), to $T_s = 4, 9, 17, 22, 39$ N m^{-1}, and $T_s = 5$ N m^{-1}, respectively. Dashed lines correspond to $T/T_s = 1$ for $p/P_s < 1$ and $T/T_s \sim (p/P_s)^{0.4}$ for $p/P_s > 1$. Inset: same as main figure but in dimensional units. For all colours, (square, star) indicate depression and (circle) overpressure.

shift of the dispersion relation is observed when the forcing is increased. The theoretical dispersion relation $\omega^2 = (D/\rho)k^5 + (T/\rho)k^3$ describes the data well when the single fitting parameter T varies from $T = 4$ N m^{-1} (top curve) at the lowest forcing amplitude up to $T = 40$ N m^{-1} (bottom curve) for the highest forcing one. This minimum value of T is consistent with the static tension T_s^0 (with no water) only due to the attaching of the sheet to the vessel (see estimation in § 3). The shift of the dispersion relation with the forcing is observed when $p > P_s^0$. For fixed P_s and a forcing amplitude such that $p \lesssim P_s$, no shift is observed in the dispersion relation (see inset of figure 3*a*). We then performed similar experiments for various applied P_s, and the value of a mean 'dynamical' tension T is deduced from the fit of the dispersion relation as in figure 3(*a*). T is plotted as a function of p, for various applied pressures P_s (and thus various T_s, from (2.5)) in the inset of figure 3(*b*), and in rescaled variables T/T_s and p/P_s in the main figure 3(*b*). Figure 3(*b*) shows the collapse of all data on a master curve displaying two regimes: for $p < P_s$, one has $T \simeq T_s$, meaning that the nonlinear effects of the waves are not strong enough to shift the dispersion relation (as in the inset of figure 3*a*). On the other hand, when $p > P_s$, T is found to increase with p as $T \sim p^{0.4}$. The inset of figure 3(*b*) shows the unrescaled variables. When the forcing p is increased, T is first constant, equal to the static tension T_s (horizontal dashed lines), and then follows the nonlinear law $T \sim p^{0.4}$ for various P_s. Note that when P_s is applied, there is no effect of the sheet curvature on the wave propagation since the wavelengths are small compared to the radius of curvature.

4.3. *Sheet tension induced by nonlinear waves*

We now explain that the observed shift of the dispersion relation is due to the mean tension induced by the waves. Let us consider a one-dimensional elastic string, fixed at both ends, subjected to an initial static force F_s with a Young modulus E' and a
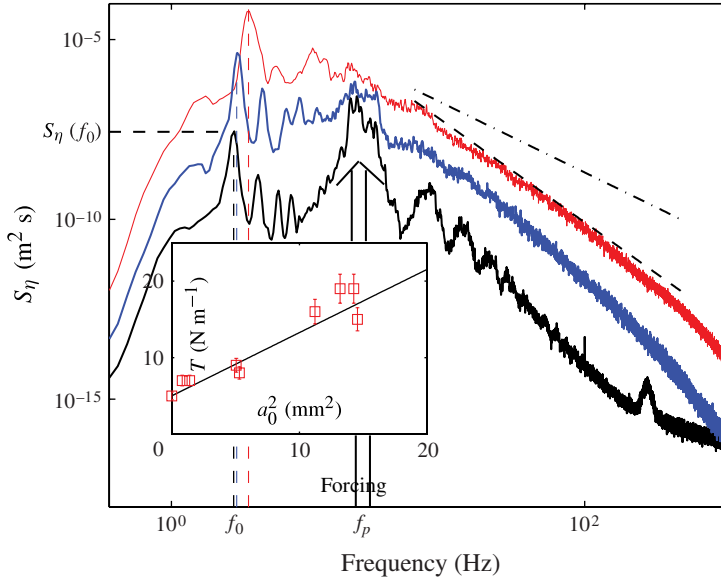
FIGURE 4. (Colour online) Frequency spectrum $S_\eta(f)$ of the wave height for increasing forcing amplitudes (bottom to top). Single-point temporal measurement. Forcing bandwidth: 7–10 Hz. $P_s = 0$ and $T_s^0 = 4$ N m^{-1}. The first vessel eigenmode (f_0, k_0), f_0 increases with the forcing (see vertical dashed lines). Sloping dashed line has a slope -4.1. Dash–dot line has a slope $-17/6$. Inset: T extracted from two-dimensional measurements as a function of the amplitude a_0 of the vessel eigenmode at f_0. Solid line is the nonlinear model (4.1) with $c = 3$ the only fitting parameter. $10 \leqslant p \leqslant 40$ Pa.

cross-section Σ. When a relatively large transverse displacement of amplitude a_0 is imposed, at wavenumber k_0, the string elongates and longitudinal waves are generated due to a geometrical nonlinearity. The latter modulate the tension force of the string as $F = F_s + F_{nl}$, with $F_{nl} \sim E'\Sigma(a_0k_0)^2$ (Morse & Ingard 1968; Legge & Fletcher 1984). F_{nl} is a nonlinear tension due to the coupling between the longitudinal and the transverse motions of the string. The nonlinear force $\sim(a_0k_0)^2$ is similar to the one involved in the radiation pressure in acoustics (Morse & Ingard 1968). Let us now apply this result for a one-dimensional elastic string to a two-dimensional elastic sheet. The tension stress T of the sheet is thus

$$T = T_s + cEh(a_0k_0)^2, \qquad (4.1)$$

with h the sheet thickness, E the Young modulus, and c a geometry-dependent dimensionless constant. Equation (4.1) is consistent with our above observations of T increasing with the forcing amplitude, if one single wave mode is experimentally involved. To identify its wavenumber k_0 and determine its amplitude a_0, long-time recording of the wave height $\eta(t)$ at a single location of the sheet is performed to resolve the low-frequency response of the system. Figure 4 shows the spectrum of $\eta(t)$ for different forcing amplitudes, and for $P_s = 0$. At low forcing (bottom curve), the forcing response (7–10 Hz) is observed as well as their harmonics. A peak is also visible at low frequency f_0 near 2 Hz (see vertical dashed black line). When the forcing is increased, the high-frequency part of the spectrum displays a frequency power law, whereas the low-frequency part shows that the peak initially at f_0 grows strongly in amplitude, and is slightly increased in frequency (see vertical dashed lines).

This peak amplitude is found to grow nonlinearly with the forcing, and becomes the most energetic frequency at high enough forcing (see the top two curves). The peak frequency f_0 corresponds to the first antisymmetric eigenmode, k_0, of a circular sheet determined by the zero of Bessel function of the first kind (Morse & Ingard 1968). We find $k_0 = 19$ m^{-1} (i.e. $\lambda_0 = 33$ cm) for $R = 20$ cm, and thus $f_0 \approx 2$ Hz using (2.2) with $T = T_s^0$.

The frequency shift of the sheet eigenmode with the amplitude is consistent with the increase of T observed above. The values of T (for the same forcing parameters as in the one-point measurements) are deduced from two-dimensional space–time measurements (see above). The amplitude a_0 of the mode k_0 is extracted from figure 4, using the relation $a_0^2(f_0) = \int_{f_0}^{f_0+\delta f} S_\eta(f)\,\mathrm{d}f$, with $\delta f = 0.06$ Hz the spectrum frequency resolution. When plotting the tension T as a function of a_0 as in the inset of figure 4, one finds that $T = T_s^0 + c' a_0^2$, with $c' = c\,Eh$ and $T_s^0 = 4$ N m^{-1}, in agreement with (4.1). As the eigenvalue frequency is much less that the elastic wave one ($5 \lesssim f \lesssim 500$ Hz), the eigenmode oscillations are quasi-static with respect to the wave propagation. To sum up, the nonlinear quasi-static oscillations of the fundamental eigenmode of the sheet induce a mean additional tension on the whole sheet.

4.4. *Scaling of tension with pressure: dynamical case*

In §4.2, we have experimentally shown that $T \sim p^{0.4}$. This scaling is explained as follows. First, assume a tension wave (of wavenumber k and amplitude a) propagating on a one-dimensional string. The power I due this transverse wave is $I \sim Fv$, with F the tension force and v the velocity of the wave. Assuming $v = \partial a/\partial t \sim a\omega$, and $F = T\partial a/\partial x \sim Tak$, one has thus $I = Ta^2\omega k$. For a large enough a, only a dynamical tension $T \gg T_s$ acts on the string. Using (4.1), that is $T \sim (ak)^2$, one has $I = T^2\omega/k$. For the dispersion relation of a one-dimensional string $\omega = \sqrt{T/\rho}k$, one finds $T \sim I^{2/5}\rho^{1/5}$. Similarly, for the dispersion relation of pure tension waves on a two-dimensional floating sheet, $\omega^2 = (T/\rho)k^3$, and one has $T \sim I^{2/5}(\rho/k)^{1/5}$. Finally, using the experimental observation $I \sim p$, one obtains $T \sim p^{2/5}(\rho/k)^{1/5}$ in good agreement with our observations of $T \sim p^{0.4}$ in figure 3 and §4.2.

5. Wave turbulence

Here, we study the regime of wave turbulence when the system is subjected to a random-noise forcing at large scale.

5.1. *Wave power spectrum*

Figure 4 shows the power spectrum of the wave height $S_\eta(f)$ as a function of frequency for different forcing amplitudes. At low forcing, the spectrum exhibits peaks at the forcing frequencies and at their harmonics. When the forcing is high enough, $S_\eta(f)$ displays a power law $\sim f^{-4.1}$ on one order of magnitude in frequency (see the sloping dashed line), and is thus found to be scale-invariant as expected for a wave turbulence regime. This power-law exponent is far from the $-17/6 \simeq -2.8$ exponent (see the dot–dash line) predicted by dimensional analysis (see (2.11)).

The spatial spectrum $S_v(k = \|\boldsymbol{k}\|)$ of the transverse velocity is computed by integrated the space–time spectrum of $S_v(\boldsymbol{k}, f)$ over all the directions of $\boldsymbol{k}$ and over f. Figure 5 shows $S_v(k)$ when the forcing is increased and for two sheet sizes. At low forcing amplitude, the forcing response is mainly observed to generate a very steep spectrum. When the forcing is further increased, energy is redistributed to higher frequencies, leading to a less steep spectrum and a regime roughly corresponding
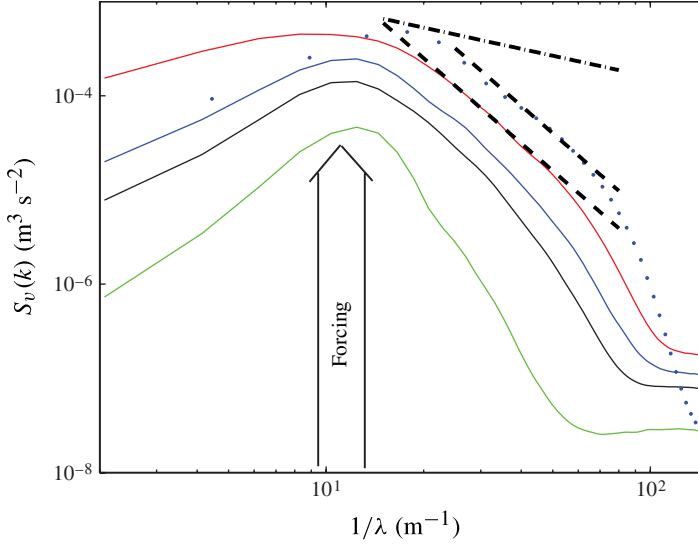
FIGURE 5. (Colour online) Spatial spectrum $S_v(k)$ of the wave transverse velocity for increasing forcing amplitudes (bottom to top). Solid lines: large vessel, forcing bandwidth 7–10 Hz. Dotted line: small vessel, forcing bandwidth 15–20 Hz. Dashed lines have a slope -3; dash–dot line has a slope $-3/4$. $10 \leqslant p \leqslant 40$ Pa.

to a power law of the spatial scales on less than one decade ($1/\lambda \approx 20$–80 m^{-1}). This power-law spectrum scales as $S_v(k) \sim k^{-\alpha}$, with $\alpha = 3 \pm 0.2$; α is found to be independent of the sheet size and the forcing bandwidth used, but is far from $-3/4$ (see dot–dash line), the value predicted by dimensional analysis (see (2.9)). Note that a power law is only reached when $p/P_S \gg 1$, i.e. when nonlinear effects become important. This observation is found whatever the static pressure is. The presence of bending waves does not explain this discrepancy since bending wave turbulence is predicted to scale as $k^{-1/4}$ (see (2.10)). Finally experimental spectrum scalings in both space and frequency suggest that the change of variable $k \longleftrightarrow f$ using the linear dispersion relation to estimate $S_v(f)$ from $S_v(k)$ is consistent. Indeed, using $S_v(\omega) = S_v(k)/(\mathrm{d}\omega/\mathrm{d}k)$ and $S_v(k) \sim k^{-3}$ found experimentally, we find $S_v(f) \sim f^{-7/3}$, thus $S_\eta \sim f^{-13/3}$ for pure tension waves ($\omega(k) \sim k^{3/2}$). This estimated exponent is consistent with the one found experimentally, $S_\eta \sim f^{-4.1}$.

5.2. *Forcing-induced anisotropy*

Isotropy of the wave field is assumed by wave turbulence theory (Newell & Rumpf 2011). The spatial spectrum $S_v(k_x, k_y, f^*)$ at a given frequency f^* is shown in figure 6 for moderate and strong forcing. The wave energy is localized around a ring in the Fourier space, the radius of which, $k^* = k(f^*)$, is given by the linear dispersion relation (2.2). At low frequency ($f^* = 20$ Hz), energy is spread in all directions (see figure 6a,c), the maximum of energy being near the forcing direction (*y*-axis). Thus, the forcing induces anisotropy at low frequency. At higher frequency ($f^* = 80$ Hz), this anisotropy is still observed for moderate forcing (see figure 6b), and becomes much more isotropic at strong forcing (see figure 6d). This is likely to be due to nonlinear interactions and multiple reflections on the vessel boundary that enables energy transfers at small scales and redistribution in all directions. Different frequencies or
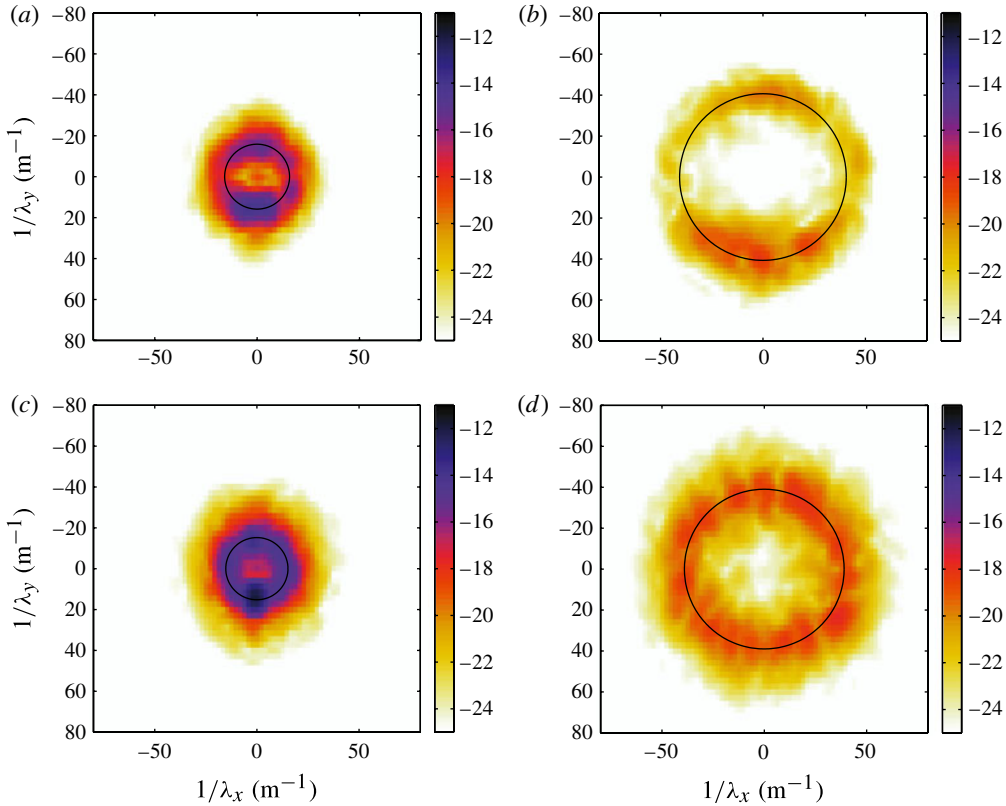
FIGURE 6. (Colour online) Space spectrum $S_v(k_x, k_y)$ at a fixed frequency $f^* = 20$ (a,c) or 80 (b,d) Hz, for a moderate (a,b) and strong forcing (c,d). Energy is localized on a circle of radius k^* given by the dispersion relation. At low frequency (a,c), the maximum of energy is localized is the forcing direction (y-axis). At high forcing and high frequency (d) the spectrum is more isotropic.

forcing conditions lead to the same conclusions: the forcing induces anisotropy at large scales, and isotropy is reached at small scales for strong enough forcing.

The spatial spectrum $S_v(k)$ of figure 5 is obtained by integrating $S_v(\boldsymbol{k})$ over all directions of $\boldsymbol{k}$. It thus averages the spectrum components in the forcing direction (y-axis) and in other directions. By integrating $S_v(\boldsymbol{k})$ over the y-axis, one gets its component in the forcing direction $S_v^y(k)$. Similarly, by integrating $S_v(\boldsymbol{k})$ over the x-axis, one gets its component in the normal direction to the forcing $S_v^x(k)$. The angle partial integration is performed with a 0.5 rad tolerance around the direction (x or y). Figure 7(a) shows $S_v(k)$, $S_v^x(k)$ and $S_v^y(k)$. As the energy maximum is localized in the y direction (see above), the maximum of $S_v^y(k)$ is almost one order of magnitude greater than $S_v^x(k)$. Moreover, all spectra display power laws, say $S_v^x(k) \sim k^{-\alpha_x}$ and $S_v^y(k) \sim k^{-\alpha_y}$, with $\alpha_x \neq \alpha_y$. More precisely, one finds $\alpha = 3 \pm 0.3$, $\alpha_x = 2.3 \pm 0.3$ and $\alpha_y = 3.5 \pm 0.5$, each being roughly independent of the forcing, p/P_s, as shown in figure 7(b), but all far from the $-3/4$ prediction of (2.9).

Computing $S_v(k, f)$ either on one quarter or on the whole spatial window leads to similar results: the wave energy is redistributed on a curve described by the theoretical dispersion relation with the same value of T. Computing $S_v(\boldsymbol{k}, f)$ integrated over all
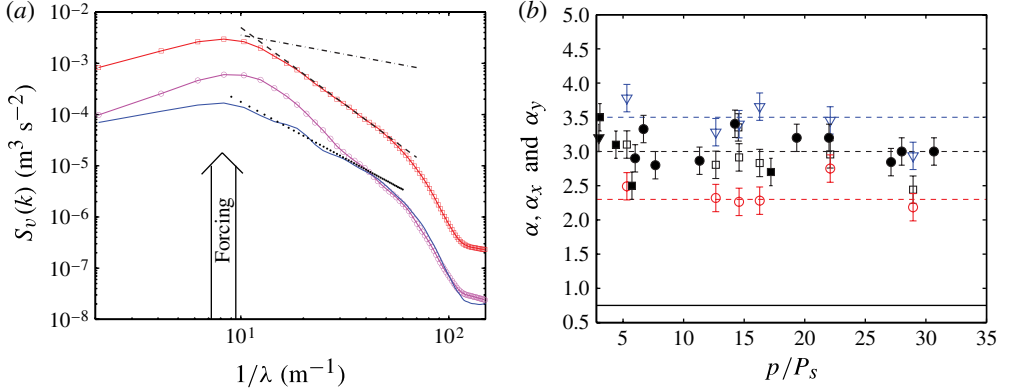
FIGURE 7. (Colour online) (*a*) Spatial spectrum $S_v(k)$ of the wave transverse velocity. $\square-$, $S_v(k)$; $\circ-$, $S_v^y(k)$; and $-$, $S_v^x(k)$. Dashed line has a slope -3; dash–dot line has a slope $-3/4$; dotted line has a slope -2.3. Large vessel, forcing bandwidth 7–10 Hz, $p = 70$ Pa. (*b*) Power-law exponents. Large vessel: $\square$, α; $\circ$, α_x; and $\triangledown$, α_y; $P_s = P_s^0 = 5$ Pa. Small vessel: α for $\bullet$, $P_s = P_s^0 = 3$ Pa; $\blacksquare$, $P_s = 7$ Pa; and $\blacktriangledown$, $P_s = 55$ Pa. Dashed lines are $\alpha_y = 3.5$, $\alpha = 3$ and $\alpha_x = 2.3$ from top to bottom (see text).

directions of $\boldsymbol{k}$ or only for some chosen directions, also gives the same value of T. Although the wave field is not isotropic at large scales, the sheet tension is thus isotropic and homogeneous as assumed theoretically in § 2.3.

To summarize, we observe an anisotropy of the wave field at large scales induced by the forcing. The spectrum computed either in the forcing direction or in the normal direction leads to different power-law scalings with k, the one in the forcing direction being the steepest, and both are in disagreement with the prediction of (2.9). When performing experiments with two wave makers with directions normal to each other, $S_v(k)$, $S_v^x(k)$ and $S_v^y(k)$ are found to be similar with the same power-law scaling in k^{-3}, still far from the $k^{-3/4}$ prediction. Thus, the anisotropy is not the main origin for this discrepancy between the theoretical and experimental exponents.

5.3. *Role of the sheet finite size*

When the vessel diameter is reduced by a factor 2, a power-law spectrum, $S_v(k) \sim k^{-\alpha}$ is still observed as shown in figure 5. Figure 7(*b*) shows α as a function of p/P_s for the small and large vessels with $\alpha = 3 \pm 0.3$ whatever the vessel size used. This value of α is also independent of the sheet tension for $3 \leqslant P_s \leqslant 60$ Pa for which a power-law spectrum is observed. The regime of wave turbulence is thus independent of the vessel size and of the static sheet tension whatever the forcing in the range $5 \leqslant p/P_s \leqslant 30$.

5.4. *Time scale separation*

Let us now consider the typical time scales involved in our experiment. Wave turbulence theory assumes a time scale separation $\tau_l(k) \ll \tau_{nl}(k) \ll \tau_d(k)$, between the linear propagation time, τ_l, the nonlinear interaction time, τ_{nl}, and the dissipation time, τ_d. The linear propagation time is $\tau_l = 1/\omega(k)$, with $\omega(k)$ the linear dispersion relation of (2.2); $\tau_d(k)$ is determined by performing freely decaying experiments (Miquel & Mordant 2011*b*); $\tau_{nl}(k)$ is related to the broadening of the dispersion relation and can be experimentally estimated by the width of the spatio-temporal spectrum $S_v(k, f)$ (Nazarenko 2011; Miquel & Mordant 2011*a*).
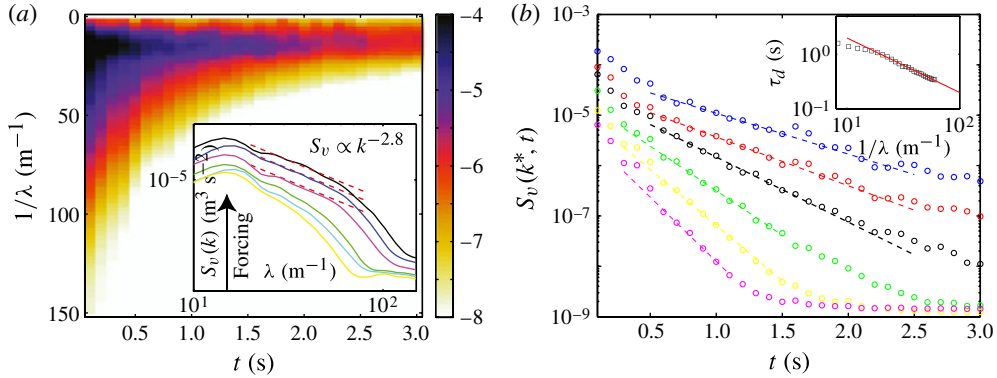
FIGURE 8. (Colour online) Temporal decay of the space–time spectrum for a sinusoidal forcing at $f_p = 20$ Hz. (a) $\langle \log S_v(k, t) \rangle$. Inset: space spectrum $\langle S_v(k, t^*) \rangle$ at different times $t^* = 0.1, 0.2, 0.4, 0.6, 0.8$ and 1 s (from top to bottom). Dashed lines have a slope -2.8. (b) ○, Temporal decay of the spectrum Fourier component $\langle S_v(k^*, t) \rangle$ at modes $k^* = 116.9, 143.2,$ 182.2, 246.3, 312.3, and 377.6 m^{-1} (from top to bottom). Dashed lines are corresponding $\exp[-t/\tau_d(k^*)]$ with $\tau_d(k^*)$ fitted from the data. Inset: τ_d versus k. □, Experiments; and —, best fit $\tau_d = Ak^{-1}$ with $A = 3.2$ s m^{-1}.

5.4.1. *Dissipation time*

The dissipation time, $\tau_d(k)$, at each scale k is determined experimentally by performing freely decaying experiments. The protocol is similar to that used in recent works on gravity–capillary wave turbulence (Deike, Berhanu & Falcon 2012) or on flexural wave turbulence on a plate (Miquel & Mordant 2011*b*). First, surface waves are generated to reach a stationary wave turbulence state (see §3). Then the forcing is stopped at $t = 0$, and the temporal decay of the spatial wave field is recorded during a time $\mathcal{T} = 3$ s. The experiment is automatically iterated 10 times to improve statistics, and results are averaged (ensemble average denoted by $\langle \cdot \rangle$). To analyse the different steps of the decay, the wave velocity spectrum is computed over short-time intervals $[t, t + \delta t]$ with $\delta t = 0.1$ s. Experiments are performed in the large vessel, and similar results are obtained whatever the forcing.

The temporal decay of the space–time power spectrum $\langle S_v(k, t) \rangle$ is displayed in figure 8(*a*) and shows that small scales are first dissipated. The inset shows the temporal evolution of the spatial spectrum $\langle S_v(k, t^*) \rangle$ at different decay times t^*. It corresponds to different vertical sections of the space–time spectrum of the main figure 8(*a*). At the beginning of the decay ($t \lesssim 0.5$ s), the spectrum shape is conserved (see top curves in the inset figure 8*a*). For $t \lesssim 0.5$ s, one finds roughly $\langle S_v(1/\lambda, t^*) \rangle \sim k^{-2.8}$ within the inertial range. This exponent is thus close to the one found in the stationary state (see §5.2). This self-similar temporal decay of the wave spectrum has been predicted theoretically (Zakharov *et al.* 1992), and has been observed for decaying capillary wave turbulence (Deike *et al.* 2012), and decaying flexural wave turbulence on a plate (Miquel & Mordant 2011*b*). For $t \gtrsim 0.5$ s, no power-law regime is observed, meaning that the wave turbulence regime stops in favour of a purely dissipative regime.

Figure 8(*b*) shows the temporal evolution of the amplitude of the Fourier modes $\langle S_v(k^*, t) \rangle$ at different k^*. It corresponds to different horizontal sections of the space–time spectrum of the main figure 8(*a*). For $t \gtrsim 0.5$ s, each Fourier mode is found to decay exponentially in time, $\langle S_v(k^*, t) \rangle \sim \exp[-2t/\tau_d(k^*)]$ with a typical
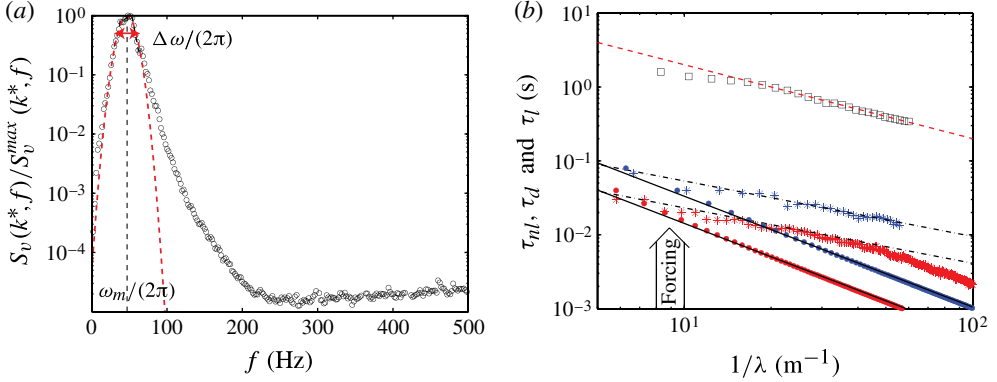
FIGURE 9. (a) ∘, Spectrum $S_v(k^*, f)$ normalized by its maximum for $k^* = 2\pi \times 29 \text{ m}^{-1}$; - - -, Gaussian fit: $\exp[-(\omega - \omega^*)^2/\Delta\omega^2]$ with $\omega^* = 2\pi \times 47 \text{ s}^{-1}$, and $\Delta\omega = 2\pi \times 14.8 \text{ s}^{-1}$. (b) Typical time scales: $*$, τ_{nl} and $\bullet$, τ_l for both low (top (blue)) and high (bottom (red)) forcing; and $\square$; τ_d. Dashed line: best fit $\tau_d \sim 1/k$; dash–dot lines: $\tau_{nl} \sim k^{-3/4}$ from (2.13); solid lines: $\tau_l \sim k^{-3/2}$ (tensional waves). Low forcing is $p = 2$ Pa, and $T = 4 \text{ N m}^{-1}$. High forcing is $p = 145$ Pa, and $T = 17 \text{ N m}^{-1}$.

time $\tau_d(k^*)$, given by the best fit of the experimental data; $\tau_d(k^*)$ is displayed in the inset of figure 8(b). We find $\tau_d(k^*) \sim 1/k^*$ meaning that small scales dissipate more rapidly than large ones. By using temporal measurement at one spatial point, one gets the frequency scaling, $\tau_d(f) \sim f^{-0.7}$, consistently with $\tau_d(k) \sim k^{-1}$ since $\omega^2 = (T/\rho)k^3$. Similar scaling laws are observed whatever the initial static tension used. Even if the physical origin of the dissipation is not known, an important result of this part of the work is that dissipation occurs at all scales within the inertial range, contrary to the hypothesis of wave turbulence theory.

5.4.2. *Nonlinear interaction time*

As shown previously in figure 2, the spatio-temporal spectrum $S_v(k, f)$ broadens around the linear dispersion relation curve when the forcing is increased. The nonlinear time scale $\tau_{nl}(k)$ is related to this broadening (Nazarenko 2011; Miquel & Mordant 2011a). It is estimated by $\tau_{nl}(k) = 1/\Delta\omega(k)$, the inverse of the width $\Delta\omega(k)$ of spectrum $S_v(k, f)$ at a given wavenumber k. As shown in figure 9(a), $\Delta\omega(k)$ is extracted from $S_v(k, f)$ by the r.m.s. value of a Gaussian fit with respect to k at a fixed ω^*. Then, iterating this protocol to all k allows us to determine $\tau_{nl}(k)$. Figure 9(b) shows that $\tau_{nl}(k)$ is found to scale as $\tau_{nl} \sim k^{-3/4}$ for low and high forcing, in good agreement with the prediction of (2.13). When the forcing is increased, the degree of nonlinearity increases, and τ_{nl} is found to decrease. This is consistent with the theoretical scaling $\tau_{nl} \sim \epsilon^{-1/2}$ of (2.13).

5.4.3. *Comparison of time scales*

We can now take stock of our results to compare the evolution of the linear time $\tau_l(k)$, the nonlinear time $\tau_{nl}(k)$, and the dissipation time $\tau_d(k)$ across the scales. We have experimentally found $\tau_{nl} \sim k^{-3/4}$ (see §5.4.2) as expected theoretically from (2.13), $\tau_d(k) \sim k^{-1}$ (see §5.4.1), whereas $\tau_l(k) \sim k^{-3/2}$ comes from the experimental dispersion relation. The time scale separation hypothesis of wave turbulence theory, $\tau_l(k) \ll \tau_{nl}(k) \ll \tau_d(k)$, is well satisfied experimentally for $k \gtrsim k_c = 2\pi \times 10 \text{ m}^{-1}$ as shown in figure 9(b) for two forcing amplitudes. For $k \lesssim k_c$, the scale separation

breaks down since $\tau_l \approx \tau_{nl} \ll \tau_d$. This scale corresponds to a wavelength $\lambda_c \simeq 10$ cm of the order of the forcing scale ($\gtrsim 10$ cm – see figure *7a*), and thus is not involved in the cascade process. Finally, even though the nonlinear time scale is in good agreement with (2.13) and though the time scale separation is well satisfied experimentally within the inertial range, the scaling of the power-law spectrum with k does not follow (2.9).

6. Conclusion

We have reported results of experiments on nonlinear waves on the surface of a fluid covered by an elastic sheet. An optical method is used to obtain the full space–time wave field. It enables us to reconstruct the dispersion relation of waves showing a transition between tension and bending waves. When the forcing is increased, a shift of the dispersion relation occurs. We show that this effect is due to an additional tension of the sheet induced by transverse nonlinear motion of a fundamental mode of the sheet.

When the system is subjected to a random-noise forcing at large scales, a regime of hydroelastic wave turbulence is observed. The spectrum of wave velocity then displays power laws of frequency and of wavenumber within an inertial range. This wave turbulence state corresponds theoretically to a direct cascade of energy flux through the scales. However, the frequency and wavenumber power-law exponents of the spectrum are found to disagree with the theoretical prediction. These exponents are found to be independent of the vessel size for the two tested configurations, of the strength of the forcing, and of the static sheet tension applied. To explain this discrepancy, several hypotheses of the theory have been experimentally tested to probe their validity domain in our experiment. Although an anisotropy of the wave field is induced by the forcing at large scales and weak forcing, it is not at the origin of this discrepancy. The time scale separation hypothesis was then experimentally tested. The dissipation time of the waves, the nonlinear interaction time and the linear time of wave propagation have been measured at each scale. The separation of these time scales is clearly observed within the inertial range of the wave turbulence cascade. However, we have found that the dissipation occurs at all scales of the cascade, contrary to the theoretical hypothesis. Although we cannot determine the physical mechanism at the origin of the dissipation, the fact that it occurs at all scales could explain the discrepancy between the experimental and theoretical scalings of the spectrum. The occurrence of dissipation at all scales induces an ill-defined inertial range between the forcing and the dissipation and has been recently shown to be responsible for such a discrepancy in flexural wave turbulence on a metallic plate (Humbert *et al.* 2013; Miquel, Alexakis & Mordant 2013). Possible non-local interactions could be also put forward, such as those involving the slow dynamics of a sheet fundamental mode that has been shown to modify the sheet tension at all scales. Moreover the possible interpretation of this mode dynamic as a condensation process, similar to what happen in two-dimensional hydrodynamic turbulence (Sommeria 1986) or in optical wave turbulence (Laurie *et al.* 2012), is an open question and deserves further study.

To conclude, a regime of wave turbulence has been observed in a new experimental system even if some theoretical hypotheses are not fulfilled. We emphasize that dissipation occurring at all scales, and non-local interactions should be included in future wave turbulence theories to give a more complete description of the experiments.

Acknowledgements

REFERENCES

BOUDAOUD, A., CADOT, O., ODILLE, B. & TOUZÉ, C. 2008 Observation of wave turbulence in vibrating plates. *Phys. Rev. Lett.* **100**, 234504.

COBELLI, P., MAUREL, A., PAGNEUX, V. & PETITJEANS, P. 2009 Global measurement of water waves by Fourier transform profilometry. *Exp. Fluids* **46**, 1037–1047.

COBELLI, P., PRZADKA, A., PETITJEANS, P., LAGUBEAU, G., PAGNEUX, V. & MAUREL, A. 2011 Different regimes for water wave turbulence. *Phys. Rev. Lett.* **107**, 214503.

CONNAUGHTON, C., NAZARENKO, S. & NEWELL, A. C. 2003 Dimensional analysis and weak turbulence. *Physica* D **184** (1–4), 86–97.

DAVYS, J. W., HOSKING, R. J. & SNEYD, A. D. 1985 Waves due to a steadily moving source on a floating ice plate. *J. Fluid Mech.* **158**, 269–287.

DEIKE, L., BERHANU, M. & FALCON, E. 2012 Decay of capillary wave turbulence. *Phys. Rev.* E **85**, 066311.

DENISSENKO, P., LUKASCHUK, S. & NAZARENKO, S. 2007 Gravity wave turbulence in a laboratory flume. *Phys. Rev. Lett.* **99**, 014501.

DÜRING, G., JOSSERAND, C. & RICA, S. 2006 Weak turbulence for a vibrating plate: can one hear a Kolmogorov spectrum? *Phys. Rev. Lett.* **97**, 025503.

FALCON, E. 2010 Laboratory experiment on wave turbulence. *Discrete Contin. Dyn. Syst.* B **13**, 819–840.

FALCON, E., LAROCHE, C. & FAUVE, S. 2007 Observation of gravity-capillary wave turbulence. *Phys. Rev. Lett.* **98** (9), 094503.

GROTBERG, J. B. & JENSEN, O. E. 2004 Biofluid mechanics in flexible tubes. *Annu. Rev. Fluid Mech.* **36**, 121–147.

HERBERT, E., MORDANT, N. & FALCON, E. 2010 Observation of the nonlinear dispersion relation and spatial statistics of wave turbulence on the surface of a fluid. *Phys. Rev. Lett.* **105**, 144502.

HUMBERT, T., CADOT, O., DURING, G., JOSSERAND, C., RICA, S. & TOUZE, C. 2013 Wave turbulence in vibrating plates: the effect of damping. *Eur. Phys. Lett.* **102**, 30002.

KOLMAKOV, G. V., BRAZHNIKOV, M. Y., LEVCHENKO, A. A., ABDURAKHIMOV, L. V., MCCLINTOCK, P. V. E. & MEZHOV-DEGLIN, L. P. 2009 Capillary turbulence on the surfaces of quantum fluids. In *Progress in Low Temperature Physics*, 16 edn. chap. 6, Elsevier.

LAMB, H. 1932 *Hydrodynamics*. Dover.

LANDAU, L. & LIFCHITZ, F. 1951 *Theory of Elasticity*. Editions Mir.

LAURIE, J., BORTOLOZZO, U., NAZARENKO, S. & RESIDORI, S. 2012 One-dimensional optical wave turbulence: experiment and theory. *Phys. Rep.* **514** (4), 121–175.

LEGGE, K. A. & FLETCHER, N. H. 1984 Nonlinear generation of missing modes on a vibrating string. *J. Acoust. Soc. Am.* **76** (1), 5–12.

MARCHENKO, A. V. & SHRIRA, V. I. 1991 Theory of two-dimensional nonlinear waves in liquid covered by ice. *Fluid Dyn.* **26**, 580–587.

MCGOLDRICK, L. F., PHILLIPS, O. M., HUANG, N. E. & HODGSON, T. H. 1966 Measurements of third-order resonant wave interactions. *J. Fluid Mech.* **25**, 437–456.

MIQUEL, B., ALEXAKIS, A. & MORDANT, N. 2013 The role of dissipation in flexural wave turbulence: from experimental spectrum to Kolmogorov–Zakharov spectrum. *Phys. Rev.* E (submitted).

MIQUEL, B. & MORDANT, N. 2011a Nonlinear dynamics of flexural wave turbulence. *Phys. Rev.* E **84**, 066607.

MIQUEL, B. & MORDANT, N. 2011*b* Nonstationary wave turbulence in an elastic plate. *Phys. Rev. Lett.* **107**, 034501.

MORDANT, N. 2008 Are there waves in elastic wave turbulence? *Phys. Rev. Lett.* **100**, 234505.

MORDANT, N. 2010 Fourier analysis of wave turbulence in a thin elastic plate. *Eur. Phys. J.* B **76**, 537–545.

MORSE, P. M. & INGARD, K. U. 1968 *Theoretical Acoustics*. Princeton University Press.

NAZARENKO, S. 2011 *Wave Turbulence*. Springer.

NEWELL, A. C., NAZARENKO, S. & BIVEN, L. 2001 Wave turbulence and intermittency. *Physica* D **152–153**, 520–550.

NEWELL, A. C. & RUMPF, B. 2011 Wave Turbulence. *Annu. Rev. Fluid Mech.* **43** (1), 59–78.

PARAU, E. & DIAS, F. 2002 Nonlinear effects in the response of a floating ice plate to a moving load. *J. Fluid Mech.* **460**, 281–305.

PEAKE, N. 2001 Nonlinear stability of a fluid-loaded elastic plate with mean flow. *J. Fluid Mech.* **434**, 101–118.

PEAKE, N. & SOROKIN, S. V. 2006 A nonlinear model of the dynamics of a large elastic plate with heavy fluid loading. *Proc. R. Soc.Lond.* A **462** (2072), 2205–2224.

SCHULKES, R. M. S. M., HOSKING, R. J. & SNEYD, A. D. 1987 Waves due to a steadily moving source on a floating ice plate. Part 2. *J. Fluid Mech.* **180**, 297–318.

SHELLEY, M. J. & ZHANG, J. 2011 Flapping and bending bodies interacting with fluid flows. *Annu. Rev. Fluid Mech.* **43** (1), 449–465.

SOMMERIA, J. 1986 Experimental study of the two-dimensional inverse energy cascade in a square box. *J. Fluid Mech.* **170**, 139–168.

SQUIRE, V. A. 2007 Of ocean waves and sea-ice revisited. *Cold Reg. Sci. Technol.* **49**, 110–133.

SQUIRE, V. A., HOSKING, R. J. & KERR, A. D. 1996 *Moving Loads on Ice Plates*. Kluwer.

SQUIRE, V. A., ROBINSON, W. H., LANGHORNE, P. J. & HASKELL, T. G. 1988 Vehicles and aircraft on floating ice. *Nature* **33**, 159–161.

TAKIZAWA, T. 1985 Response of a floating sea ice sheet to a steadily moving load. *J. Geophys. Res.* **93**, 5100–5112.

WATANABE, E., UTSUNOMIYA, T. & WANG, C. M. 2004 Hydroelastic analysis of pontoon-type vlfs: a literature survey. *Engng Struct.* **26** (2), 245–256.

WRIGHT, W. B., BUDAKIAN, R. & PUTTERMAN, S. J. 1996 Diffusing light photography of fully developed isotropic ripple turbulence. *Phys. Rev. Lett.* **76**, 4528–4531.

XIA, H., SHATS, M. & PUNZMANN, H. 2010 Modulation instability and capillary wave turbulence. *Eur. Phys. Lett.* **91** (1), 14002.

ZAKHAROV, V. E., FALKOVITCH, G. C. & LVOV, V. S. 1992 *Kolmogorov Spectra of Turbulence. I. Wave Turbulence*. Springer.